Reflective Silver Thin Film Electrodes from Commercial Silver(I) Triflate *via* Aerosol-Assisted Chemical Vapor Deposition

*Sebastian C. Dixon, Joe A. Manzi, Michael J. Powell, Claire J. Carmalt and Ivan P. Parkin**

Materials Chemistry Centre, Department of Chemistry, University College London, 20 Gordon Street, London, WC1H 0AJ, UK.

*Corresponding author, E-mail: i.p.parkin@ucl.ac.uk ; Fax: +44 (0)20 769 7463 ; Tel.: +44 (0)20 7679 4669.

Abstract

The growth of metallic silver films by aerosol-assisted chemical vapor deposition at atmospheric pressure for use as thin film electrodes or reflective layers in optoelectronic stacks has been studied using the self-metallization of silver(I) trifluoromethanesulfonate (silver(I) triflate, $[Ag(SO_3CF_3)]$) during chemical vapor deposition under nitrogen, air and 5% H_2/N_2. The deposition behaviour of the triflate from a methanolic solution was observed with respect to film thickness between 170 and 240 nm, while the dependence of electrical resistivity between $\rho = 2.8 \times 10^0$ and 5.0×10^{-5} Ω cm on nanocrystallite diameter between 38 and 44 nm indicated a grain boundary-limited charge carrier propagation mechanism arising from insular film growth. Furthermore, increased nanocrystallite size reduced specular optical reflectance from 11 to 3 %. The thermal stability of silver(I) triflate as compared with other silver precursors enabled deposition at elevated temperatures with maximum growth rates of 11 nm min^{-1}, representing a manifold increase over many previously reported Ag thin film chemical vapor deposition processes on non-metallic substrates. Nanocrystallite diameter was directly proportional to film thickness, such that control over thickness enabled control over surface texture, electrical resistivity and specular optical reflectivity.

1. Introduction

Metallic silver thin films are highly useful and pervasive materials on account of their exceedingly low electrical resistivity ($\rho = 10^{-4}$-10^{-6} Ω cm), high reflectance in the

visible and near IR range, and antimicrobial activity. As such, they can be found within devices spanning a wide range of applications such as low thermal emissivity coatings,[1] giant magnetoresistant multilayer structures,[2] antimicrobial coatings in biomedical appliances,[3] and as low work function reflective electrodes in photovoltaic cells,[4] information displays[5] and, more recently, flexible[6] and transparent[7] optoelectronics. Silver film deposition is usually achieved by electrodeposition,[2] metal-organic chemical vapor deposition (MOCVD)[8] or magnetron sputtering (MS),[1,3,4] though of these, only CVD offers textured silver films as-deposited due to the island growth process,[9–11] which is particularly desirable for photovoltaic and antimicrobial applications.[12] It is generally expedient for industrially-scalable deposition processes to minimize cost by avoiding vacuum deposition methods such as MOCVD and MS, however atmospheric-pressure thermal CVD (APCVD) of silver films is virtually unheard of due to a lack of available precursors with suitably high vapor pressures.[8] High-performance silver thin films have been deposited at atmospheric pressure using flame-assisted CVD (FACVD),[13] however this technique is typically limited to small-scale sample preparation due to significant temperature variations, and therefore non-uniformity in the deposited films, being intrinsic to the method.[14]

Aerosol-assisted chemical vapor deposition (AACVD) is an atmospheric-pressure alternative to thermal APCVD which avoids the requirement of thermal APCVD that precursors should be appreciably volatile by instead generating an aerosol from a solution of the precursor.[15,16] It follows that AACVD enables a safer and wider selection of precursors, without many of the inherent hazards associated with thermal CVD precursors such as being corrosive, explosive, highly flammable or posing a risk to human health *via* inhalation.[14,17,18] AACVD has thus enabled the deposition of a range of films of metallic,[9,10] polymeric[19,20] and metal-oxide[21–23] compositions. Until now, AACVD of silver films has largely been led by Molloy *et al.*,[24–26] having been achieved by an exhaustive process of precursor preparation, with mixed results with regard to film contamination, conductivity and reflectivity. Molloy *et al.* have identified several precursors to silver film deposition on glass which successfully yield reflective and/or electrically conductive films. A summary of the best-performing Ag film precursors from the literature is given in Table 1. An arbitrary Figure-of-Merit (FOM) related to Haacke's equation[27] has here been devised to quantify the best combination of the two most desirable properties of silver films, optical reflectance and electrical resistivity, such that FOM = R/ρ, where R is the

reflectance as a percentage and ρ is the electrical resistivity. Films deposited using silver(I) perfluorobutyrate and silver(I) perfluorooctanoate had some of the best resistivities (ρ=3.8×10^{-6} and 3.8×10^{-5} Ω cm, respectively), though were not reflective. Phosphine-substituted Ag(I) complexes gave the best FOM, with FOM = 8.9×10^6 and 20×10^6 Ω^{-1} cm^{-1} for 1,1,1-trifluoro-2,4-pentanedionato(triphenylphosphine)silver(I) and 1,1,1,5,5,5-hexafluoro-4-(*n*-hexylimino)-2-pentanonato(triphenylphosphine)silver(I) respectively. In all cases however, the onset of thermal decomposition in the range 100-200 °C meant that depositions could only be carried out at relatively low temperature and thus, with AACVD being a diffusion-limited process (precursor vapor adsorption to substrate, migration of precursor to nucleation site, then desorption of by-products),[17] the film growth rates were low. In addition, no authors have yet been successful in reporting AACVD of both electrically conductive and optically reflective thin films from a commercially readily available silver precursor, such as silver pivalate, silver acetate[25] or silver nitrate.[28] From this assessment, it appears that fluorinated organosilver precursors are particularly favourable for metallic silver deposition, and indeed have previously been studied for their self-metallising decomposition pathways by which the silver component is reduced by its ligands.[8,29] However, metal trifluoromethanesulfonates (triflates) have hitherto been largely overlooked for CVD applications, in spite of appearing to be favourable for AACVD due to their high thermal stability and solubility,[23,30,31] as well as being cheap, safe and easy to handle and store, and readily commercially available. In this paper we thus explore the deposition of reflective and electrically conductive metallic silver thin films directly onto glass substrates *via* AACVD from silver(I) triflate, the structure of which is shown in Figure 1.
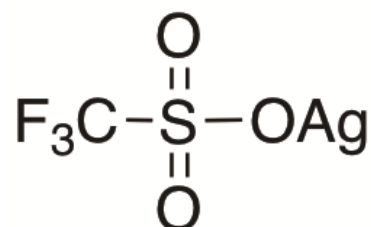
$$F_3C-\overset{\displaystyle O}{\underset{\displaystyle O}{\overset{\|}{\underset{\|}{S}}}}-OAg$$

Figure 1 Structure of silver(I) trifluoromethanesulfonate (triflate).

Table 1 Literature review spanning all known studies of Ag film deposition by AACVD where electrical resistivity ρ and total reflectance R% are quantified. Commercial availability was determined based on mainstream chemical suppliers' catalogues.

Precursor	Substrate	Commercially available?	Impurities	Resistivity $/10^{-6}$ Ω cm	R%[a]	FOM[b] $/10^6$	Growth rate /nm min^{-1}	Reference
Ag(tfac)(PPh$_3$)	Glass	N	C	7.0	62.5	8.9	1.6	Molloy 1999[24]
Ag(hfac)(PPh$_3$)	Glass	N	C, P	569	0.3	0.001	1.0	Molloy 1999[24]
Ag(hfacNhex(PPh$_3$))	Glass	N	C	3.2	64.7	20	1.6	Molloy 1999[24]
Ag(hfacNchex(PPh$_3$))	Glass	N	C	414	51.4	0.12	1.9	Molloy 1999[24]
Ag(O$_2$CC$_3$F$_7$)	Glass	N	C	3.8	0.5	0.13	0.3	Molloy 2002[25]
Ag(O$_2$CC$_6$F$_{13}$)	Glass	N	C, F	38	4.9	0.13	0.9	Molloy 2002[25]
Ag(O$_2$CBut)(PMe$_3$)$_2$	Glass	N	C, P	459	0.7	0.002	1.4	Molloy 2002[25]
HHC=CH(CH$_2$)$_2$CO$_2$Ag{P(C$_6$H$_5$)$_3$}$_2$	Glass	N	C, O	238	51	0.21	2.5	Molloy 2003[26]
H$_3$CCH=C(CH$_3$)CO$_2$Ag{P(C$_6$H$_5$)$_3$}$_2$	Glass	N	C, O, P	269	49	0.18	2.6	Molloy 2003[26]
^{n}BuB(CH$_2$PPh$_2$)$_3$Ag(PEt$_3$)	Steel	N	B, C, P	2.5	-	-	16	Marks 2008[9]
Ag(OSO$_2$CF$_3$)	Glass	Y	C, Cl, S	50	63	1.3	11	(This work)

[a]Reflectance at λ = 550 nm; [b]FOM = Figure of Merit, R%/ρ.

2. Experimental section

2.1. Materials

Silver(I) trifluoromethanesulfonate (triflate) was obtained from Aldrich and used as supplied. Nitrogen carrier gas (N_2, 99.99%), hydrogen (5% H_2/N_2) and compressed air were bought from BOC and used as supplied. Methanol (99.5%) was obtained from Merck Millipore and also used as supplied. The float glass substrate (50 × 145 × 4 mm) had a 50 nm SiO_2 barrier layer and was supplied by NSG Pilkington Ltd..

2.2. General procedure

In a typical experiment, silver(I) triflate (0.5 g, 2 mmol) was dissolved in methanol (30 mL) with stirring for *ca.* 10 min. The precursor solution was transferred to a glass bubbler for deposition. Glass substrates were cleaned prior to deposition with detergent, isopropyl alcohol and acetone in order to remove grease and debris from the surface. The apparatus used for the deposition of silver films is illustrated in a schematic in Figure 2. The substrate was positioned within the quartz tube enclosure of the reactor, atop a graphite heating block fitted with a Whatman cartridge heater regulated by a platinum-rhodium thermocouple. A sheet of stainless steel (4.5 × 15 cm) was supported at a height of 8 mm above the glass substrate to facilitate laminar flow over the glass. The reactor was heated to its target temperature at a rate of 15 °C min^{-1}, at which point the carrier gas of choice was allowed to flow through the reactor for *ca.* 1 min before the precursor was atomized using a Johnson Matthey Liquifog® piezoelectric atomizer. The precursor vapor was transported by the carrier gas at a flow rate of 1.0 L min^{-1} first through 8 mm gauge PTFE (polytetrafluoroethylene) piping to a brass baffle manifold and then through into the horizontal-bed cold-walled reactor chamber, at which point thermal decomposition of the precursor occurred to result in film growth on the glass substrate. Deposition of the films typically took *ca.* 40 min, at which point the humidifier and heating element were switched off and the substrate was allowed to cool naturally under the continuing flow of the carrier gas. Removal of the samples from the chamber occurred once the temperature had cooled to below 100 °C, at which point they were handled in open air.
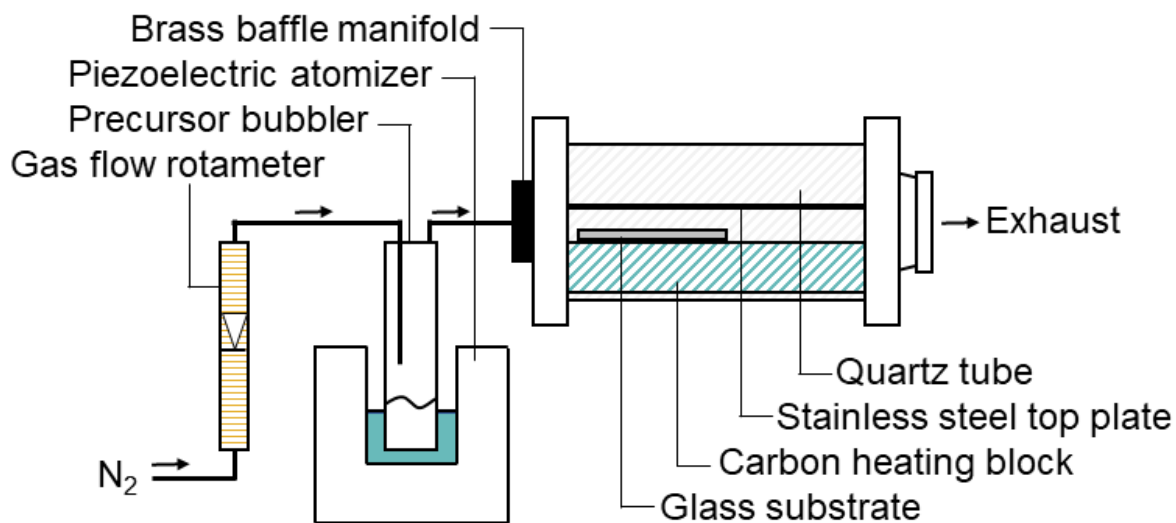
Figure 2 Schematic for apparatus used for aerosol-assisted chemical vapor deposition of thin films onto glass substrates.

2.3. Characterization details

Thermogravimetric analysis (TGA) was performed under helium using a Netzsch STA 449 C Jupiter Thermo-microbalance in an open aluminium oxide crucible.

X-ray diffractograms were taken at a glancing angle (θ = 0.8-1.0 °) in an air atmosphere on a Bruker D8 Discover diffractometer using monochromatic Cu $K_{\alpha 1}$ and $K_{\alpha 2}$ radiation wavelengths of 1.54056 and 1.54439 Å respectively, at a voltage of 40 kV and a current of 40 mA. Diffraction readings were measured between angles 2θ = 10-66°.

X-ray photoelectron spectroscopy was conducted on a Thermo Scientific K-alpha spectrometer with monochromated Al K_{α} radiation, a dual beam charge compensation system and constant pass energy of 50 eV (spot size 400 µm). Survey scans were collected in the binding energy range 0–1200 eV. High-resolution scans were used for Ag (3d), O (1s), S (2p) and C (1s). Data was calibrated against C1s (284.5 eV) and fitted using CASA XPS software.

Specular reflectance was carried out using a Filmetrics F20 spectral reflectance system against a Si wafer standard.

Scanning electron microscope images were recorded on a JEOL JSM-6301F SEM at an acceleration voltage of 5 kV.
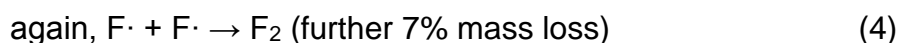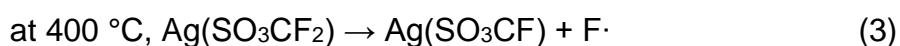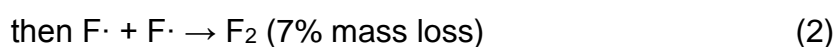
Hall effect measurements were taken at room temperature using the van der Pauw four-point probe configuration in order to determine the resistivity of the films. The measurements were performed on an Ecopia HMS-3000 instrument with a 0.58 T permanent magnet and a current of 1 µA, using square-cut coupons (*ca.* 1 × 1 cm) of the deposited films.

3. Results

3.1. Thermogravimetric analysis of the silver(I) triflate precursor

Thermogravimetric analysis (TGA) was used to determine the decomposition behaviour of the silver(I) triflate precursor at high temperature under an inert (He) atmosphere; the resulting mass loss curve and its first derivative are shown in Figure 3. All mass loss occurred between 380 and 485 °C, totalling a loss of 48%. The full range measured is shown in Figure S1. The first derivative of the mass loss curve with respect to temperature reveals three distinct stages of mass loss with sharp losses at 394 and 400 °C, followed by a broader stage spanning 460-480 °C. The first stage effects a sharp loss in mass of about 6%, then at the second a loss of 7% is seen. The final stage is a broader range over which around 30% is lost to yield the stable final product of decomposition, which constitutes 52% of the initial mass; while Ag constitutes 42% of the mass of the molecule, the remaining 10% can be accounted for as non-volatile contaminants, primarily C, which occur under the anaerobic decomposition of silver(I) triflate and are later accounted for in the X-ray photoelectron spectroscopic (XPS) elemental analysis of the films. A comparable study of anaerobic thermal decomposition of silver(I) triflate is unavailable, however the silver(II) triflate has previously been studied by anaerobic TGA with tandem mass spectrometry (MS). Malinowski *et al.* found that upon thermal decomposition, silver(II) triflate evolved gases with *m/z* signatures characteristic of SO_3, C_2F_6 and $(CF_3)_2SO_3$.[32] However, they also found that the onset of silver(II) triflate started at a much lower temperature than the silver(I) compound, beginning at 139 °C compared with 380 °C observed here. Deconvolution of the decomposition pattern here is open to speculation; it should not be assumed that the silver(I) and silver(II) triflates decompose in the same manner. There is no evidence to suggest that C_2F_6 or $(CF_3)_2SO_3$ are formed upon decomposition of silver(I) triflate; indeed, both species require sufficient stability of $CF_3\cdot$ radical species for diffusion to result in recombination either with other $CF_3\cdot$ radicals to form C_2F_6, or at neighbouring triflate species to form $(CF_3)_2SO_3$. We

7

suggest that the higher stoichiometry of triflate species in the silver(II) triflate as well as its lower decomposition temperature makes those processes more likely to occur in silver(II) than silver(I) triflate, and that the higher temperature of silver(I) triflate decomposition allows instead for formation of F· radicals and therefore F_2 evolution. Loss of each F atom from the silver(I) triflate unit effects a 7% mass loss, as such we propose that the initial two mass loss phases can be attributed to loss of the first two F atoms from the triflate, such that:

$$\text{at 394 °C, } Ag(SO_3CF_3) \rightarrow Ag(SO_3CF_2) + F· \qquad (1)$$

$$\text{then } F· + F· \rightarrow F_2 \text{ (7% mass loss)} \qquad (2)$$

$$\text{at 400 °C, } Ag(SO_3CF_2) \rightarrow Ag(SO_3CF) + F· \qquad (3)$$

$$\text{again, } F· + F· \rightarrow F_2 \text{ (further 7% mass loss)} \qquad (4)$$

Following these two stages is a broader phase with about 30% mass loss, in which much of the remainder of the triflate species is lost. SO_2 accounts for 25% of the mass of silver(I) triflate however the species formed upon decomposition of the SO_3CF species are open to speculation.
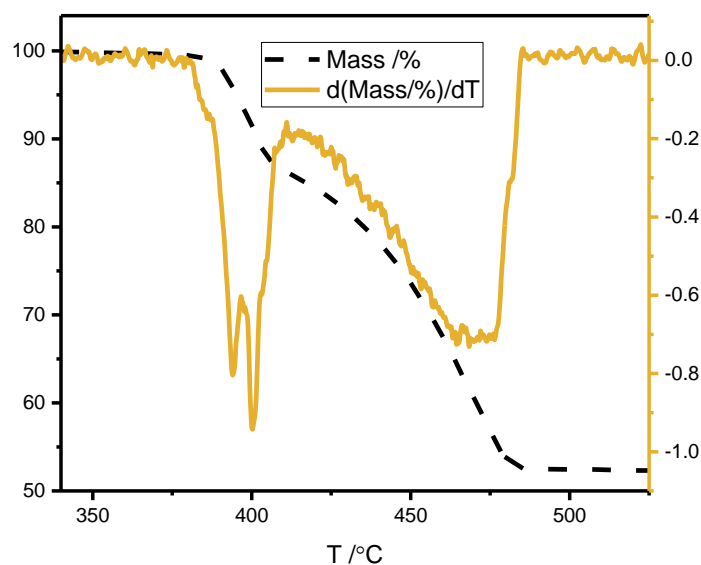
Figure 3 Thermogravimetric analysis of the silver(I) triflate precursor, with the first derivative of the mass loss curve shown to illustrate significant stages of decomposition. The mass loss curve is corrected for temperature-dependent buoyancy using a linear fit to the low-temperature region.

3.2. Scanning electron microscopy

Metallic silver films were deposited onto SiO_2-coated glass substrates from a methanol solution of silver(I) triflate *via* aerosol-assisted chemical vapor deposition (AACVD). Deposition occurred primarily on the glass lower plate, though thermophoretic effects lead to increased deposition on the steel upper plate with increasing substrate temperature.[19] Nitrogen was primarily used as the carrier gas, though depositions under air or a 5% H_2/N_2 mixture were also carried out, as summarized in Table 2. The horizontal-bed nature of the AACVD reactor used here resulted in a variation of thickness spanning the length and width of the substrate. In the table given, comparisons are made between the thickest points of each film, typically a 1 × 1 cm^2 area, 2 cm from the reactor inlet in the centre of the glass.

9

Table 2 Summary of deposition conditions explored in optimization of silver film deposition from silver(I) triflate.

Carrier gas	T /°C[a]	d /nm[b]	Resistivity /10^{-6} Ω cm	R%[c]	Appearance
N_2	450	-	∞	47	Brown, transparent
N_2	550	450	50	63	White at thickest region, silvery at periphery
N_2	600	180	7.3×10^4	44	Silvery, translucent
Air	550	-	∞	26	Brown at thickest region, yellow at periphery, transparent
5% H_2/N_2	550	-	$>10^9$	30	Silvery, dark

[a]*Substrate temperature;* [b]*film thickness determined by cross-sectional SEM, blanks where indeterminable;* [c]*total reflectance at λ = 550 nm.*

Scanning electron microscopy (SEM) shown in Figure 4 revealed a highly textured surface for all films. This is suggestive of a Volmer-Weber island growth mechanism which is typical for films grown *via* AACVD, and is indicative of a greater affinity of the precursor towards the growing film than towards the substrate.[33] Cross-sectional SEM enabled thickness measurements of the films. Examples of these are shown in Figure 4. Blanks appear in Table 2 where discontinuity of the film impeded reliable thickness determination. In comparing the top-down micrographs with the thicknesses, it becomes clear that thicker films yield larger grains, with a broadening particle size distribution with increasing thickness where smaller particles grow atop a base of larger interconnecting grains. This is a typical pattern for thin film growth arising from insular grain growth.[26] Top-down and cross-sectional micrographs for a wider range of film thicknesses are shown in Figure S2.
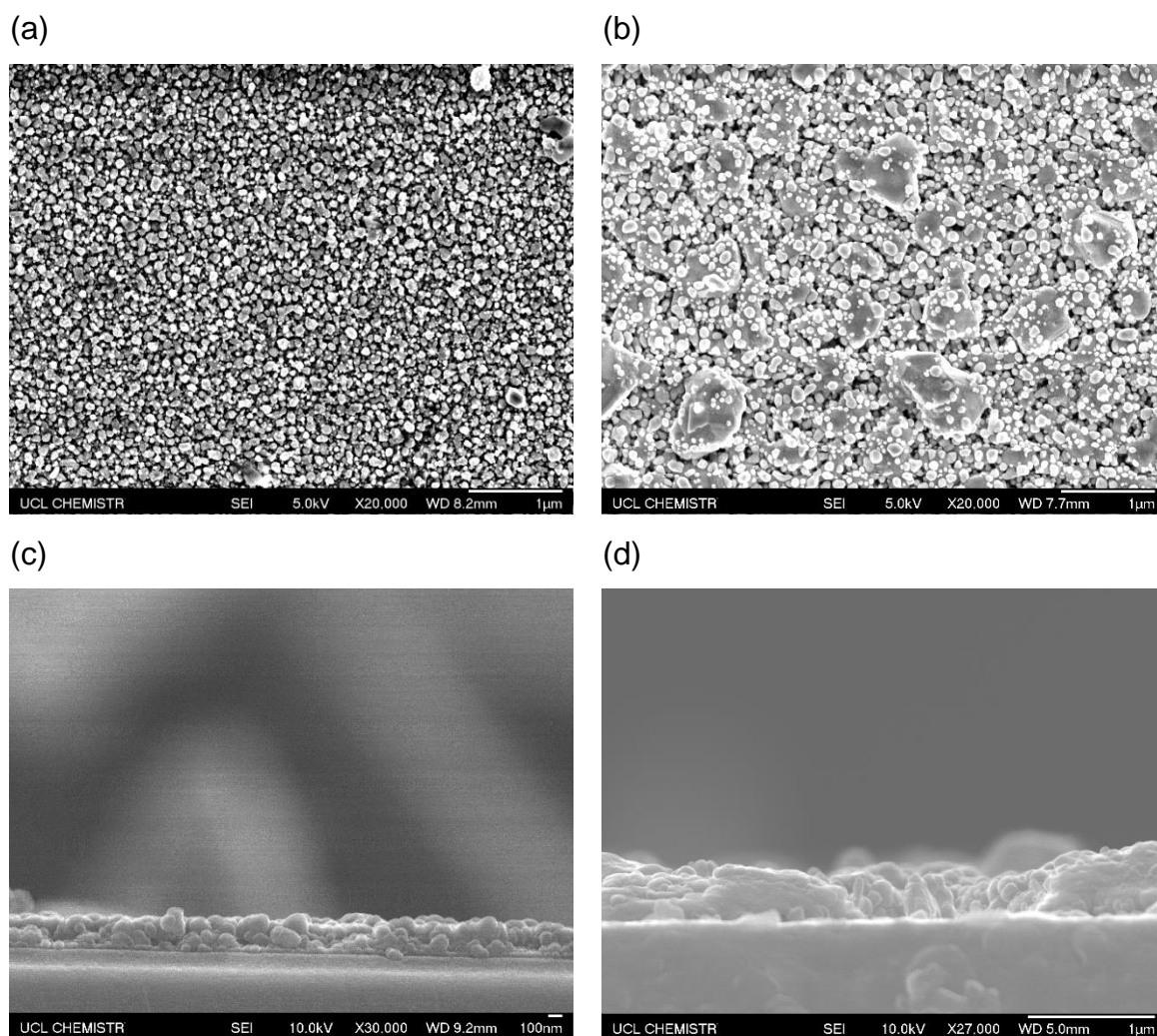
Figure 4 Scanning electron micrographs of metallic silver films deposited at 550 °C under N_2, with thicknesses of (a, c) 225±5 nm and (b, d) 390±30 nm, shown (a, b) top-down at 20 000× magnification, with (c, d) cross-sectional images shown at 30 000 and 27 000× respectively.

Deposition under air yielded yellow-brown, strongly-adhered transparent films with no conductivity, which in the SEM were revealed to have irregular grain size and shape distribution, with no connectivity between grains (see Figure S3). The transparency is evident in the transmission spectra shown in Figure S4. The occurrence of irregular agglomerated features when depositing in the presence of O_2 may be due to premature oxidation of the organic portion of the precursor, leading to Ag nucleation in the vapor phase rather than at the substrate surface. With film growth suppressed, Ag clusters may instead partially diffuse into the substrate, becoming embedded and granting mechanical resistance of the Ag against abrasion. Ag diffusion into metal-oxide substrates has been observed before by Kulczyk-Malecka

et al. and is particularly prevalent in the temperature range 500-600 °C.[34] On the other hand, deposition under the hydrogen mixture yielded adherent but dark mirror-like films with a narrow distribution of small-size grains and poor conductivity (see Figure S3), while lacking resistance to abrasion. This variability in film characteristics is typical of Ag film growth and is attributed largely to the microstructure – grain connectivity determines electrical characteristics, while grain size and spatial distribution determines colour and specular reflectivity and transmittance.[26,35,36] In general, the resistance to mechanical abrasion of silver films on oxide substrates is poor due to weak wetting between the noble metal and the dipolar surface beneath.[9] Deposition under a nitrogen flow of 1.0 L min^{-1} at 550 °C yielded similarly adherent films with the best combination of electrical conductivity and reflectivity; a photograph showing an example of such a film is shown in Figure 5. The thickest such films were 450 nm thick as determined by cross-sectional SEM, corresponding to a nominal growth rate of *ca.* 11 nm min^{-1}. This represents a manifold increase over most other depositions of Ag films by AACVD (see **Table 1**) and we attribute this observation to the thermal stability of the triflate precursor, which enables deposition at elevated temperatures and therefore enhanced precursor diffusion processes and subsequent film growth.[18] The superior performance of those films deposited under nitrogen was such that they form the focus of this work, although analysis of films deposited in the presence of air or H_2 is also carried out where explicitly noted herein.

Figure 5 Photograph showing mirror-like silver film grown from silver(I) triflate on glass under nitrogen.

3.3. Elemental analysis by X-ray photoelectron spectroscopy

X-ray photoelectron spectroscopy (XPS) was carried out to determine the elemental composition of the Ag films. All films demonstrated Ag^0 as the only environment in the Ag3d region regardless of the carrier gas used in the deposition, as shown in Figure 6(a-c). Binding energies of the $Ag3d_{5/2}$ peaks were at 368.0 eV (±0.3 eV), closely matching previously observed values for metallic Ag.[37,38] The strongly self-metallising behaviour of the silver(I) triflate precursor was reinforced by the occurrence of the Ag^0 state to the exclusion of higher Ag oxidation states, even when depositing under air.
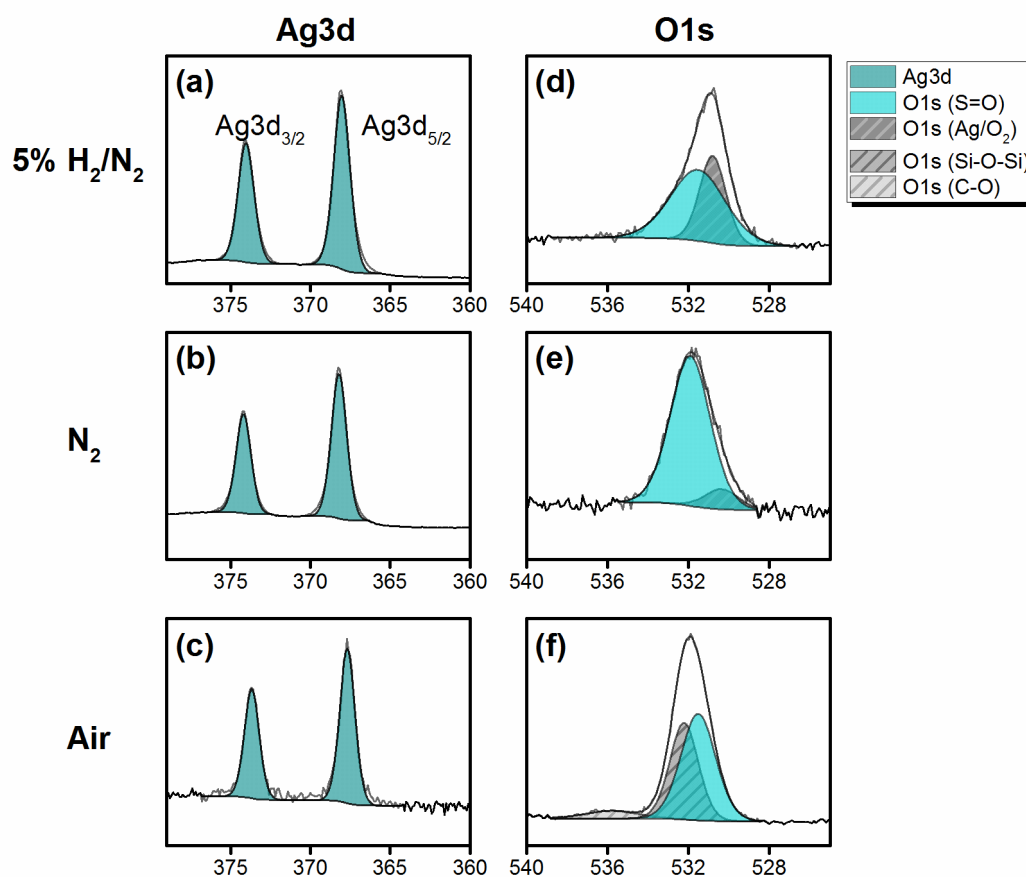

Figure 6 Surface X-ray photoelectron spectra for (a-c) Ag3d and (d-f) O1s environments for metallic silver films deposited from silver(I) triflate synthesized under (a, d) 5% H_2/N_2, (b, e) N_2 and (c, f) air carrier gases. All films displayed only the Ag^0 oxidation state. The O1s environment is deconvoluted into S=O from residual triflate

precursor, physisorbed O_2/Ag, C-O from partially oxidized triflate residue near the surface and bridging Si-O-Si arising from the substrate beneath.

The O1s spectra, shown in Figure 6(d-f), lacked any Ag_xO environment, therefore supporting the presence of only an Ag^0 state. The O1s peaks were deconvoluted to reveal a total of four O environments, one of which had a binding energy of 530.5±0.2 eV, attributed to O_2 physisorbed on Ag.[39,40] In all spectra the strongest O1s peak occurred at 531.7±0.2 eV, attributed to S=O groups in residual triflate precursor at the film surface, and its relative intensity was diminished in films deposited in the presence of reactive gases H_2 or O_2, shown in Figure 6(d) and (f) respectively. Two other environments present in the O1s region were only observed in films deposited under air, occurring around 532.2 and 536.1 eV and were attributed to bridging Si-O-Si from the exposed underlying silica substrate and C-O groups in partially oxidized triflate residue respectively. These assignments were assisted by a diminishing intensity of both the S=O and Ag/O_2 O1s peaks with Ar ion beam etching, with a concomitant increase in the Si-O-Si O1s peak (see Figure S5), while the high-binding energy peak at 536.1 eV agrees with previously observed O1s environments in fluorinated hydrocarbons at 535.9 eV.[41] These were also supported by the exclusive emergence of Si peaks and other glass species in survey scans of air-deposited films (see Figure S6 and S7). The S2p^{3}/$_2$ peak, shown in Figure S7, occurred at 161.6±0.2 eV, congruous with the occurrence of organic S previously reported to appear at 161.5 eV.[42] This ruled out the occurrence of Ag_2S, which usually appears at 160.7 eV,[43] in agreement with the lack of an Ag(I) signal.

Depth profiling was carried out by etching the films using an Ar^+ ion beam, scanning for the Ag3d, C1s, O1s (surface O-Ag and substrate O-Si), S2p and Si2p at each level. These are summarized in Figure 7, with the same carried out for a film deposited using 5% H_2/N_2 for comparison. Previous work[8,44] finds that Ag deposition with a small quantity of H_2 assists in the reduction of halide contamination due to the formation of hydrogen halides, though there was no trace of F in any films deposited here, regardless of carrier gas. In the case of deposition from silver trifluoroacetate, hydrogen fluoride was reported form preferentially over C_xH_y such that solid C is co-deposited with Ag.[44] Overall, S contamination levels in both samples were highest near to the surface of the film, falling from 11 at% at the surface in both films to 2.8-4.9 and 0.5-2.3 at% S:(Ag+S) for deposition with and without the addition of H_2,

respectively. C was the most significant contaminant in the bulk, with 19-27 and 12-17 at% C:(Ag+C) with and without H_2, respectively. In the case of both C and S contamination, for silver(I) triflate deposition it seems that addition of H_2 to the carrier flow increases film contamination. The most likely reason for this is the discouragement of the oxidation to volatile species of C and S-containing by-products of the deposition by the methanol solvent in the presence of H_2. The occurrence of C and S contaminants in the bulk was expected from the TGA data shown in Section 3.1, where 10 wt% of the organic portion of the silver(I) triflate molecule remained in the resultant metallic Ag under anaerobic decomposition. The particularly high C contamination in films deposited in the presence of H_2 is the most likely reason for their high resistivity, with $\rho > 10^3$ Ω cm compared with the 10^{-5} to 10^{-2} Ω cm range spanned when depositing in N_2. Likewise their dark appearance and small grain size are attributed to this high degree of carbon contamination.
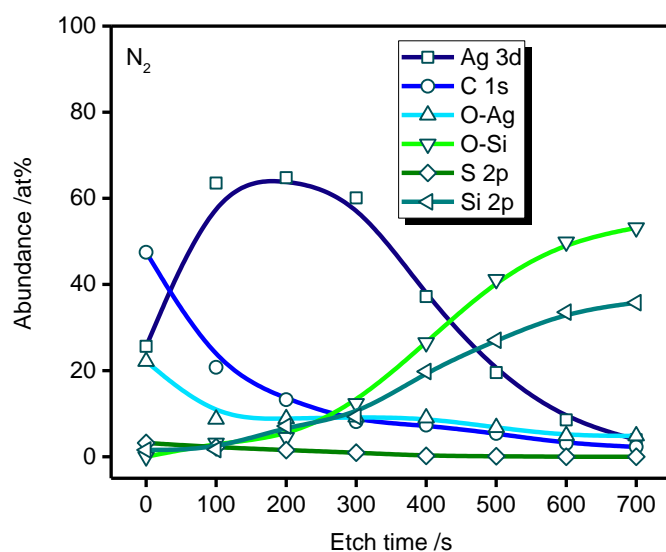
(a)
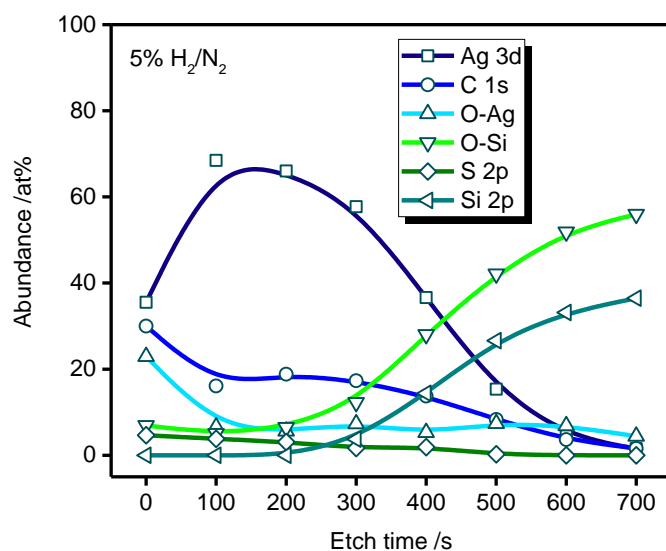
(b)

Figure 7 XPS Ar-etch depth profiling of Ag films deposited at 550 °C using (a) N_2 and (b) 5% H_2/N_2 carrier gases. O-Ag and O-Si refer to physisorbed contaminant on the Ag surface and the underlying substrate, respectively.

3.4. X-ray diffractometry

X-ray diffraction (XRD) patterns were typical of metallic Ag thin films which usually grow preferentially along the (111) direction, as evident in a representative diffractogram shown in Figure 8(a),[45] to the exclusion of other Ag_xO crystallographic phases. Crystallite sizes within the silver films were determined from the width of the

(111) peak in the XRD patterns *via* the Scherrer equation,[46] shown in Figure 8(b). Here, the Scherrer equation takes the form:

$$d = \frac{k\,\lambda}{\Delta(2\theta)\,cos\theta_{111}} \qquad (5)$$

where *d* is the crystallite diameter, *k* is the Scherrer constant equal to 0.9, *λ* is the wavelength of incident X-ray radiation in nm, *Δ(2θ)* is the full-width at half-maximum of the (111) peak in radians and *θ*$_{111}$ is the Bragg angle in radians. It has been observed previously that increased crystallite size is concurrent with thicker film deposition,[47] which is likewise observed in the relationship illustrated in Figure 8(c). Error in film thickness was determined using the standard error, $SE = \frac{SD}{\sqrt{n}}$ where SD is the standard deviation of n number of measurements, of multiple (at least three) thickness measurements across the length (ca. 1 cm) of each sample. We found that this method was a significant source of error (ca. 5-10 % margin), and since we were able to demonstrate a correlation between film thickness and XRD-determined crystallite diameter in Figure 8(c), the crystallite diameters have been used in drawing correlations with physical properties instead of thicknesses. Crystallite diameters estimated using the Scherrer equation consistently returned diameters to within ca. 0.5 nm (1-2 % error margin). While it is likely that there will be some instrumental error in their absolute determination, all samples were measured under the same conditions using the same instrument so should be self-consistent and therefore provide a useful tool for correlating crystallite diameters to other physical properties such as specular reflectance.
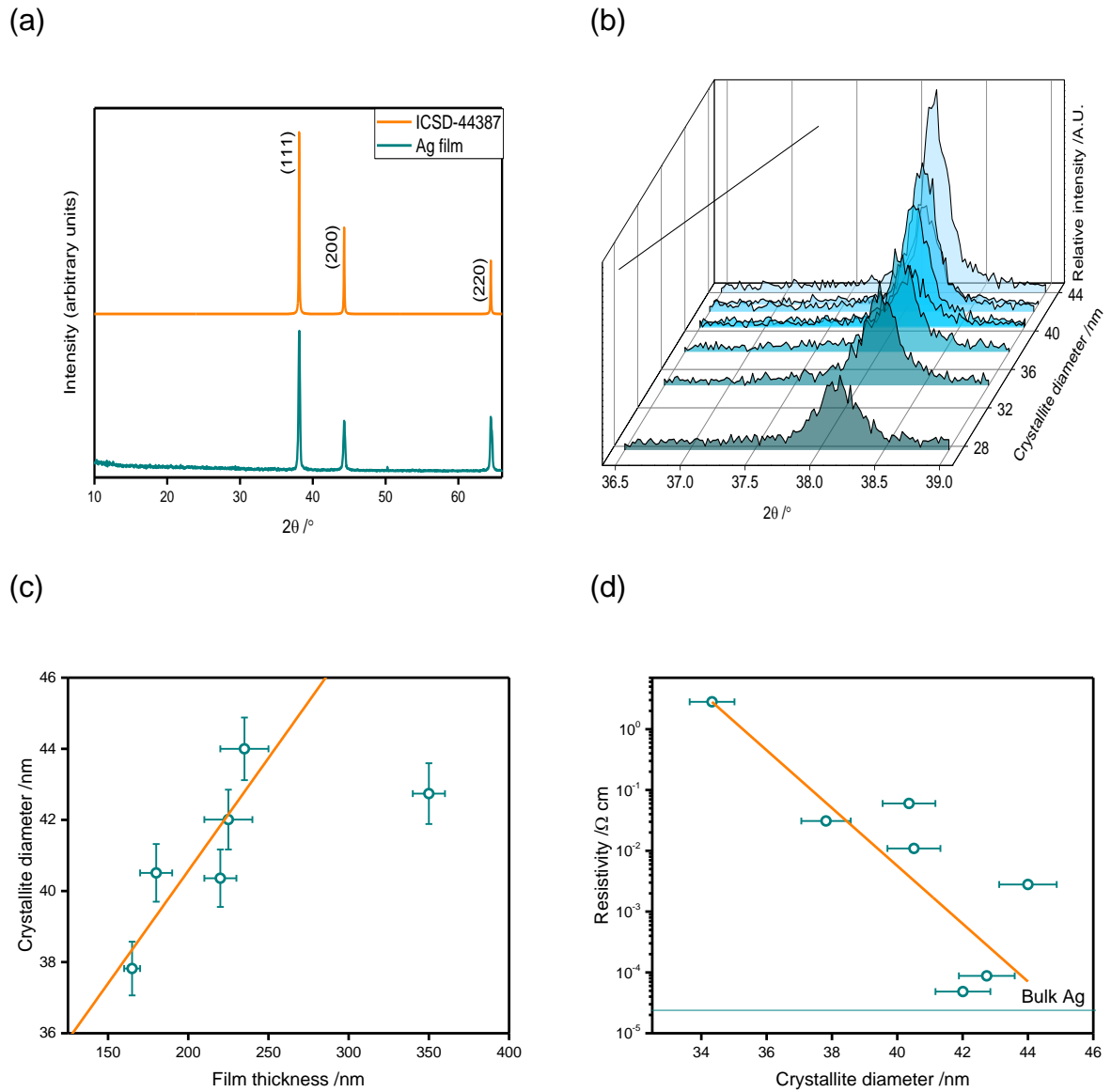
Figure 8 X-ray diffractometry of metallic silver films deposited at 550 °C under N_2, showing (a) a representative diffraction pattern across the full 2θ range measured alongside the reference powder pattern (ICSD-44387), (b) comparison of the (111) peak used in the determination of crystallite diameters, which are (c) shown against film thicknesses (coefficient of determination R^2 = 0.66). (d) A clear trend then arises between electrical resistivity in the Ag films and increasing crystallite diameter, as determined using Hall effect measurements (R^2 = 0.93).

3.5. Electrical properties

Electrical resistivity measurements, where resistivity $\rho = dR_s$ with d as film thickness and R_s as sheet resistance, were carried out in the van der Pauw

configuration using a Hall effect instrument. Calculation of the resistivity enables comparison of the intrinsic properties of films of different thicknesses, while sheet resistance is an extrinsic property dependent on thickness and morphology. The bulk resistivity of silver has been reported as 1.6×10^{-6} Ω cm.[35] Looking at Figure 8(d) it is clear that the electrical resistivity is reduced with increasing crystallite diameter (which is itself concomitant with increasing film thickness). Since increasing the crystallite diameter effects a reduction in the ratio of the grain boundary area to the grain volume, grain boundary scattering is likewise reduced such that the film becomes more 'bulk-like' with increasing thickness. This indicates that charge carrier propagation in Ag thin films is a grain boundary-limited process, with film resistivity gradually moving toward the Ag bulk resistivity of 1.6×10^{-6} Ω cm as crystallites become larger.[35] Indeed, this is a well-known property of polycrystalline metallic films and also applies to Al, Co, Ni, Pd and Au films.[48] The lowest measured resistivity here of $\rho = 5.0 \times 10^{-5}$ Ω cm is comparable with polycrystalline metallic silver films sputter-deposited in previous studies.[35]

3.6. UV-visible spectroscopy

While thinner samples to the naked eye appeared mirror-like, thicker samples approaching 400 nm were white and matte in appearance, indicative of a developed surface microstructure which scatters visible light. This effect assists with the light-trapping mechanism in photovoltaic devices, where minimization of reflective losses is conducive to increased device efficiency.[49] In order for visible light to be scattered, surface features ought to be of similar dimension to the wavelength of the light (*ca.* 400-750 nm), while samples with smaller surface features would be expected to effect less scattering of visible light.[50] Likewise, a correlation can be drawn between mean crystallite diameters as determined by XRD and specular reflectivity in Figure 9 whereby smaller crystallites comprise a film with a higher degree of specular reflectance. The apparent shift of a resonance maximum towards longer wavelengths with increasing crystallite diameter is typical of the transition of silver films from insular to continuous and is attributed to increasing electron mean free path length in the films.[51,52]
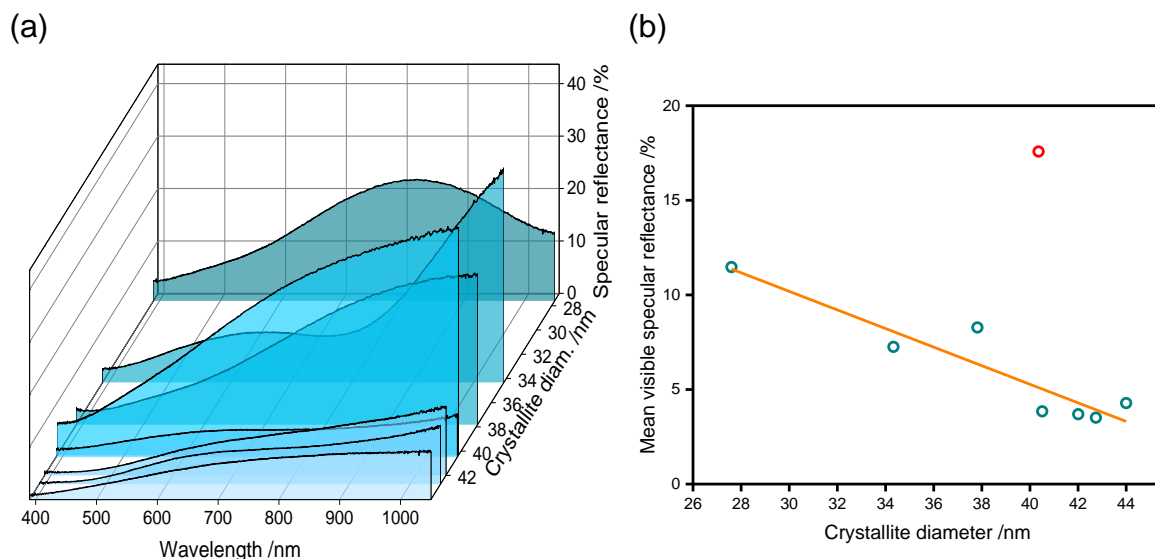
Figure 9 (a) Specular reflectance spectra of metallic silver thin films 550 °C deposited under N_2 with increasing crystallite diameters, (b) their mean specular reflectance in the visible region (400-750 nm) shown against their crystallite diameters ($R^2 = 0.87$).

4. Conclusion

The self-metallization of silver(I) triflate has been adopted for the aerosol-assisted chemical vapor deposition of metallic silver thin films on glass at atmospheric pressure. As compared with air or 5% H_2 in N_2, an inert nitrogen deposition environment was found to be best suited in order to obtain the most desirable properties of low contamination and high electrical conductivity, with deposition carried out at 550 °C. The effect of varying crystallite diameter from 38 to 44 nm was studied by varying film thickness from 170 to 240 nm, with the outcome of reducing electrical resistivity from $\rho = 2.8 \times 10^0$ to 5.0×10^{-5} Ω cm and specular reflectance from 11 to 3 %. Elemental analysis revealed that the silver(I) triflate precursor is strongly self-metallising and yields exclusively the metallic phase, even when depositing in air. Deposition using silver(I) triflate occurred at a maximum observed growth rate of 11 nm min^{-1}, a manifold increase over many previously reported Ag thin film chemical vapor deposition processes on non-metallic substrates. The presented method for deposition of metallic silver films is facile, uses a low-cost readily commercially-available precursor and provides a means of obtaining metallic silver films with microstructural control.

5. Acknowledgements

Supporting information available with full thermogravimetric analysis of the silver(I) triflate precursor, UV-vis-IR transmission data, scanning electron micrographs of films deposited under different carrier gases and for thickness determination, and impurity analysis by X-ray-photoelectron survey spectra and O1s and S2p$^{3}/_{2}$ peak modelling.

6. References

(1)   Ando, E.; Suzuki, S.; Aomine, N.; Miyazaki, M.; Tada, M. Sputtered Silver-Based Low-Emissivity Coatings with High Moisture Durability. *Vacuum* **2000**, *59*, 792–799.

(2)   Valizadeh, S.; Holmbom, G.; Leisner, P. Electrodeposition of Cobalt–silver Multilayers. *Surf. Coatings Technol.* **1998**, *105*, 213–217.

(3)   Rebelo, R.; Manninen, N. K.; Fialho, L.; Henriques, M.; Carvalho, S. Morphology and Oxygen Incorporation Effect on Antimicrobial Activity of Silver Thin Films. *Appl. Surf. Sci.* **2016**, *371*, 1–8.

(4)   Sai, H.; Jia, H.; Kondo, M. Impact of Front and Rear Texture of Thin-Film Microcrystalline Silicon Solar Cells on Their Light Trapping Properties. *J. Appl. Phys.* **2010**, *108*, 044505.

(5)   Cao, W.; Li, J.; Chen, H.; Xue, J. Transparent Electrodes for Organic Optoelectronic Devices: A Review. *J. Photonics Energy* **2014**, *4*, 040990.

(6)   Guillén, C.; Herrero, J. TCO/Metal/TCO Structures for Energy and Flexible

Electronics. *Thin Solid Films* **2011**, *520*, 1–17.

(7)   Shrotriya, V.; Li, G. Translucent Solar Cell. US20090229667 A1, 2009.

(8)   Samoilenkov, S.; Stefan, M.; Wahl, G.; Paramonov, S.; Kuzmina, N.; Kaul, A. Low Temperature MOCVD of Conducting, Micrometer-Thick, Silver Films. *Chem. Vap. Depos.* **2002**, *8*, 74–78.

(9)   McCain, M. N.; Schneider, S.; Salata, M. R.; Marks, T. J. Tris(Phosphino)Borato Silver(I) Complexes as Precursors for Metallic Silver Aerosol-Assisted Chemical Vapor Deposition. *Inorg. Chem.* **2008**, *47*, 2534–2542.

(10) Panneerselvam, A.; Malik, M. A.; O'Brien, P.; Helliwell, M. The Aerosol-Assisted CVD of Silver Films from Single-Source Precursors. *Chem. Vap. Depos.* **2009**, *15*, 57–63.

(11) Noor, N.; Chew, C. K. T.; Bhachu, D. S.; Waugh, M. R.; Carmalt, C. J.; Parkin, I. P. Influencing FTO Thin Film Growth with Thin Seeding Layers: A Route to Microstructural Modification. *J. Mater. Chem. C* **2015**, *3*, 9359–9368.

(12) Franken, R. H.; Stolk, R. L.; Li, H.; van der Werf, C. H. M.; Rath, J. K.; Schropp, R. E. I. Understanding Light Trapping by Light Scattering Textured Back Electrodes in Thin Film N-i-p-Type Silicon Solar Cells. *J. Appl. Phys.* **2007**, *102*, 014503.

(13) Sheel, D. W.; Brook, L. A.; Yates, H. M. Controlled Nanostructured Silver Coated Surfaces by Atmospheric Pressure Chemical Vapour Deposition. *Chem. Vap. Depos.* **2008**, *14*, 14–24.

(14) Choy, K. Chemical Vapour Deposition of Coatings. *Prog. Mater. Sci.* **2003**, *48*, 57–170.

(15) Knapp, C. E.; Carmalt, C. J. Solution Based CVD of Main Group Materials.

Chem. Soc. Rev. **2016**, *45*, 1036–1064.

(16) Marchand, P.; Hassan, I. A.; Parkin, I. P.; Carmalt, C. J. Aerosol-Assisted
      Delivery of Precursors for Chemical Vapour Deposition: Expanding the Scope
      of CVD for Materials Fabrication. *Dalt. Trans.* **2013**, *42*, 9406.

(17) Powell, M. J.; Carmalt, C. J. Aerosols: A Sustainable Route to Functional
      Materials. *Chem. - A Eur. J.* **2017**, *23*, 15543–15552.

(18) Powell, M. J.; Potter, D. B.; Wilson, R. L.; Darr, J. A.; Parkin, I. P.; Carmalt, C.
      J. Scaling Aerosol Assisted Chemical Vapour Deposition: Exploring the
      Relationship between Growth Rate and Film Properties. *Mater. Des.* **2017**,
      129, 116–124.

(19) Dixon, S. C.; Peveler, W. J.; Noor, N.; Bear, J. C.; Parkin, I. P.
      Superhydrophobic Au/Polymer Nanocomposite Films via AACVD/Swell
      Encapsulation Tandem Synthesis Procedure. *RSC Adv.* **2016**, *6*, 31146–
      31152.

(20) Zhuang, A.; Liao, R.; Lu, Y.; Dixon, S. C.; Jiamprasertboon, A.; Chen, F.;
      Sathasivam, S.; Parkin, I. P.; Carmalt, C. J. Transforming a Simple
      Commercial Glue into Highly Robust Superhydrophobic Surfaces via Aerosol-
      Assisted Chemical Vapor Deposition. *ACS Appl. Mater. Interfaces* **2017**,
      acsami.7b13182.

(21) Dixon, S. C.; Jiamprasertboon, A.; Carmalt, C. J.; Parkin, I. P. Luminescence
      Behaviour and Deposition of Sc 2 O 3 Thin Films from Scandium(III)
      Acetylacetonate at Ambient Pressure. *Appl. Phys. Lett.* **2018**, *112*, 221902.

(22) Dixon, S. C.; Sathasivam, S.; Williamson, B. A. D.; Scanlon, D. O.; Carmalt, C.
      J.; Parkin, I. P. Transparent Conducting N-Type ZnO:Sc – Synthesis,
      Optoelectronic Properties and Theoretical Insight. *J. Mater. Chem. C* **2017**, *5*,

7585–7597.

(23) Manzi, J. A.; Knapp, C. E.; Parkin, I. P.; Carmalt, C. J. Aerosol Assisted Chemical Vapour Deposition of Transparent Conductive Aluminum-Doped Zinc Oxide Thin Films from a Zinc Triflate Precursor. *Thin Solid Films* **2016**, *616*, 477–481.

(24) Edwards, D. A.; Harker, R. M.; Mahon, M. F.; Molloy, K. C. Aerosol-Assisted Chemical Vapour Deposition (AACVD) of Silver Films from Triphenylphosphine Adducts of Silver β-Diketonates and β-Diketoiminates, Including the Structure of [Ag(Hfac)(PPh$_3$)]. *J. Mater. Chem.* **1999**, *9*, 1771–1780.

(25) Edwards, D. A.; Harker, R. M.; Mahon, M. F.; Molloy, K. C. Aerosol-Assisted Chemical Vapour Deposition (AACVD) of Silver Films from Triorganophosphine Adducts of Silver Carboxylates, Including the Structure of [Ag(O$_2$CC$_3$F$_7$)(PPh$_3$)$_2$]. *Inorganica Chim. Acta* **2002**, *328*, 134–146.

(26) Edwards, D. A.; Mahon, M. F.; Molloy, K. C.; Ogrodnik, V. Aerosol-Assisted Chemical Vapour Deposition of Silver Films from Adducts of Functionalised Silver Carboxylates. *J. Mater. Chem.* **2003**, *13,* 563–570.

(27) Ginley, D. S.; Hosono, H.; Paine, D. C. *Handbook of Transparent Conductors*; 2010.

(28) Ponja, S. D.; Sehmi, S. K.; Allan, E.; MacRobert, A. J.; Parkin, I. P.; Carmalt, C. J. Enhanced Bactericidal Activity of Silver Thin Films Deposited via Aerosol-Assisted Chemical Vapor Deposition. *ACS Appl. Mater. Interfaces* **2015**, *7*, 28616–28623.

(29) Xu, C.; Hampden-Smith, M. J.; Kodas, T. T. Aerosol-Assisted Chemical Vapor Deposition (AACVD) of Silver, Palladium and Metal Alloy (Ag$_{1-x}$Pd$_x$, Ag$_{1-x}$Cu$_x$ and Pd$_{1-x}$Cu$_x$) Films. *Adv. Mater.* **1994**, *6*, 746–748.

(30)   Yanagihara, N.; Nakamura, S.; Nakayama, M. A Thermal Study of Several Lanthanide Triflates. *Polyhedron* **1998**, *17*, 3625–3631.

(31)   Raisbeck, D.; Hurst, S. J.; Parkin, I. P.; Carmalt, C. J.; Manzi, J. A. Deposition Process. WO 2016132100 A1, 2016.

(32)   Malinowski, P. J.; Mazej, Z.; Derzsi, M.; Jagličić, Z.; Szydłowska, J.; Gilewski, T.; Grochala, W. Silver(Ii) Triflate with One-Dimensional [Ag(Ii)(SO3CF3)4/2]∞ Chains Hosting Antiferromagnetism. *CrystEngComm* **2011**, *13*, 6871.

(33)   Binions, R.; Parkin, I. P. Novel Chemical Vapour Deposition Routes to Nanocomposite Thin Films. *Adv. Nanocomposites - Synth. Charact. Ind. Appl.* **2007**, 611–638.

(34)   Kulczyk-Malecka, J.; Kelly, P. J.; West, G.; Clarke, G. C. B.; Ridealgh, J. A.; Almtoft, K. P.; Greer, A. L.; Barber, Z. H. Investigation of Silver Diffusion in TiO2/Ag/TiO2 Coatings. *Acta Mater.* **2014**, *66*, 396–404.

(35)   Guillén, C.; Herrero, J. Plasmonic Characteristics of Ag and ITO/Ag Ultrathin Films as-Grown by Sputtering at Room Temperature and after Heating. *J. Phys. D. Appl. Phys.* **2013**, *46*, 295302.

(36)   Long, Y.; Wang, Y.; Liu, Y.; Zeng, Q.; Li, Y. Maintenance of the Activity of Mono-Dispersed Au and Ag Nano-Particles Embedded in Agar Gel for Ion-Sensing and Antimicrobial Applications. *Sci. China Chem.* **2015**, *58*, 666–672.

(37)   Kaushik, V. K. XPS Core Level Spectra and Auger Parameters for Some Silver Compounds. *J. Electron Spectros. Relat. Phenomena* **1991**, *56*, 273–277.

(38)   Gao, X.-Y.; Wang, S.-Y.; Li, J.; Zheng, Y.-X.; Zhang, R.-J.; Zhou, P.; Yang, Y.-M.; Chen, L.-Y. Study of Structure and Optical Properties of Silver Oxide Films by Ellipsometry, XRD and XPS Methods. *Thin Solid Films* **2004**, *455–456*, 438–442.

(39)   Boronin, A. .; Koscheev, S. .; Zhidomirov, G. . XPS and UPS Study of Oxygen States on Silver. *J. Electron Spectros. Relat. Phenomena* **1998**, *96*, 43–51.

(40)   Bukhtiyarov, V. I.; Carley, A. F.; Dollard, L. A.; Roberts, M. W. XPS Study of Oxygen Adsorption on Supported Silver : Effect of Particle Size. *Surf. Sci.* **1997**, *381*, L605–L608.

(41)   Clark, D. T.; Feast, W. J.; Tweedale, P. J.; Thomas, H. R. ESCA Applied to Polymers. XXVI. Investigation of a Series of Aliphatic, Aromatic, and Fluorine-Containing Polycarbonates. *J. Polym. Sci. Polym. Chem. Ed.* **1980**, *18*, 1651–1664.

(42)   Mullins, D. R.; Lyman, P. F. Adsorption and Reaction of Methanethiol on Ruthenium(0001). *J. Phys. Chem.* **1993**, *97*, 12008–12013.

(43)   Yu, X.-R.; Liu, F.; Wang, Z.-Y.; Chen, Y. Auger Parameters for Sulfur-Containing Compounds Using a Mixed Aluminum-Silver Excitation Source. *J. Electron Spectros. Relat. Phenomena* **1990**, *50*, 159–166.

(44)   Shapiro, M. J.; Lackey, W. J.; Hanigofsky, J. A.; Hill, D. N.; Carter, W. B.; Barefield, E. K. Chemical Vapor Deposition of Silver Films for Superconducting Wire Applications. *J. Alloys Compd.* **1992**, *187*, 331–349.

(45)   Kapaklis, V.; Poulopoulos, P.; Karoutsos, V.; Manouras, T.; Politis, C. Growth of Thin Ag Films Produced by Radio Frequency Magnetron Sputtering. *Thin Solid Films* **2006**, *510*, 138–142.

(46)   Patterson, A. L. The Scherrer Formula for X-Ray Particle Size Determination. *Phys. Rev.* **1939**, *56*, 978–982.

(47)   Cai, K.; Müller, M.; Bossert, J.; Rechtenbach, A.; Jandt, K. D. Surface Structure and Composition of Flat Titanium Thin Films as a Function of Film Thickness and Evaporation Rate. *Appl. Surf. Sci.* **2005**, *250*, 252–267.

(48) De Vries, J. W. C. Temperature and Thickness Dependence of the Resistivity of Thin Polycrystalline Aluminium, Cobalt, Nickel, Palladium, Silver and Gold Films. *Thin Solid Films* **1988**, *167*, 25–32.

(49) Shah, A. V.; Schade, H.; Vanecek, M.; Meier, J.; Vallat-Sauvain, E.; Wyrsch, N.; Kroll, U.; Droz, C.; Bailat, J. Thin-Film Silicon Solar Cell Technology. *Prog. Photovoltaics Res. Appl.* **2004**, *12*, 113–142.

(50) Rossi, G.; Altavilla, C.; Scarfato, P.; Ciambelli, P.; Incarnato, L. Deposition of Transparent and Flexible Nanolayer Barrier on Standard Coating Materials for Photovoltaic Devices. *Surf. Coatings Technol.* **2014**, *239*, 200–205.

(51) Santbergen, R.; Temple, T. L.; Liang, R.; Smets, A. H. M.; Swaaij, R. A. C. M. M. van; Zeman, M. Application of Plasmonic Silver Island Films in Thin-Film Silicon Solar Cells. *J. Opt.* **2012**, *14*, 024010.

(52) Alvarez, M. M.; Khoury, J. T.; Schaaff, T. G.; Shafigullin, M. N.; Vezmar, I.; Whetten, R. L. Optical Absorption Spectra of Nanocrystal Gold Molecules. *J. Phys. Chem. B* **1997**, *101*, 3706–3712.